

Torsional dynamics and parametric instability in integrated electric drive systems with PMSM and gear train

Donglin Zhang¹, Rupeng Zhu², Luqiang Ma³

^{1,3}School of Intelligent Manufacturing, Nanjing Vocational College of Information Technology, Nanjing, 210023, China

²College of Mechanical and Electrical Engineering, Nanjing University of Aeronautics and Astronautics, Nanjing, 210016, China

¹Corresponding author

E-mail: ¹zhangdl@njcit.cn, ²rpzhu_nuaa@163.com, ³malq@njcit.cn

Received 23 March 2025; accepted 2 October 2025; published online 21 October 2025
DOI <https://doi.org/10.21595/jve.2025.24914>



Copyright © 2025 Donglin Zhang, et al. This is an open access article distributed under the Creative Commons Attribution License, which permits unrestricted use, distribution, and reproduction in any medium, provided the original work is properly cited.

Abstract. This study investigates the vibrational stability and torsional vibration characteristics of an integrated electric drive system composed of a permanent magnet synchronous motor (PMSM) and a two-stage gear pair under parametric excitation. An electromechanically coupled nonlinear torsional dynamic model is established, incorporating electromagnetic effects and time-varying mesh stiffness. The method of multiple scales is employed to analyze the parametric excitation-induced vibrational stability of the system, and the Runge-Kutta method is used to solve the vibrational differential equations and examine the dynamic response characteristics. The results indicate that the system exhibits significant coupled vibrational behavior: the spectrum of the dynamic meshing force contains not only the meshing frequency of the current gear pair but also the system's natural frequencies and meshing frequency components from other gear stages. Under conditions without external excitation, the system is found to exhibit not only primary resonance responses due to time-varying mesh stiffness excitation but also various nonlinear vibrational phenomena such as subharmonic resonance, superharmonic resonance, and combination resonance. The response is particularly pronounced near twice the first-order natural frequency.

Keywords: Integrated electric drive system, nonlinear dynamics, parametric instability, multi-scale method, electromechanical coupling.

Nomenclature

k_r	Torsional stiffness
k_m	Meshing stiffness
F_s	Magnetomotive force of the stator
F_r	Magnetomotive force of the rotor
T_e	Electromagnetic torque
W	The air gap magnetic field energy
Λ_0	Air gap permeance
u_0	Vacuum magnetic permeability
Ω_m	Meshing frequency
γ_m	Meshing phase
ϵ_m	Contact ratio
c_m	Mesh damping
c_z	Torsional damping
e_m	Comprehensive error
NVH	Noise, vibration, and harshness
PMSM	Permanent magnet synchronous motor

MMF	Magnetomotive force
Stator	Stationary part containing copper windings
Rotor	Rotating part containing permanent magnets
Winding	The set of insulated copper coils placed in the slots of the stator core
Meshing phase	The relative positional relationship of multiple gear pairs during their meshing cycle process

1. Introduction

The gear train within the reducer achieves speed reduction, converting the high-speed rotation of the motor or other power source into low-speed, high-torque output. It is widely used in fields such as automotive, construction machinery, and aerospace. The integration of the reducer and motor can reduce weight and volume of the system, lower manufacturing costs, and enhance power density. However, this integration also results in complex torsional vibrations due to the coupled excitation of electromagnetic forces and gear meshing. Therefore, studying the vibration characteristics of the integrated system is of significant importance.

Many studies have investigated the vibration response characteristics of gear systems arising from factors such as gear clearances, errors, and time-varying meshing stiffness. Shen et al. [1] developed a dynamic model of a spur gear pair considering time-varying stiffness and clearance, and analyzed the effects of multiple harmonics on periodic solutions using numerical method and the incremental harmonic balance method. Khabou et al. [2] employed the Newmark method to compute the dynamic response, performed a parameter study on spur gears driven by motors and engines, and discussed how speed variations influence the system's vibration characteristics.

Han et al. [3] employed an improved interval harmonic balance method to investigate the dynamics of a single-mesh gear system, incorporating the nonlinear effects of backlash and time-varying meshing stiffness, and examined the influence of parameter uncertainties on the system's vibration characteristics. Chen et al. [4] developed a nonlinear dynamic model of gear pairs that accounts for microscopic tooth surface features, and analyzed the effects of tooth surface roughness, viscous damping, and meshing stiffness on the dynamic behavior of the gear transmission.

Cao et al. [5] proposed a dynamic model for spur gears considering the influence of load-dependent time-varying meshing stiffness, backlash, and tooth profile deviation. The predicted response of the model was validated against experimental results. To account for axial deviation as an interval parameter in dynamic response analysis, Hu et al. [6] employed an interval analysis method based on the Chebyshev inclusion function to investigate the excitation effect of shaft alignment uncertainty on gear systems.

Extensive research has been conducted on parametric instability in gear systems induced by time-varying meshing stiffness. Parker et al. [7-9] analyzed instability in two-stage gears, planetary gears, and idler gear systems using the asymptotic perturbation method, and revealed the influence of key parameters on the instability regions and vibration response. Rao et al. [10] incorporated both time-varying meshing stiffness and shaft torsional flexibility to investigate torsional instability in a two-stage gear system. The instability regions of the gear system were analyzed using the multi-scale method, and the results were validated through numerical calculations.

Liu et al. [11] developed a dynamic model that accounts for time-varying stiffness of bearings and gear pairs, and investigated the parametric instability induced by the combined fluctuations in stiffness. Gawande et al. [12-13] used a two-stage gear train to identify specific operating conditions leading to parametric instability. The influence of meshing stiffness parameters – including mesh frequency, amplitude of stiffness variation, and mesh phasing contact ratio – on these instabilities was analyzed. The analysis was verified through numerical solution, demonstrating that replacement gear pairs with appropriate mesh phasing can eliminate the instability regions originally present in the two gear pairs of the two-stage gear transmission

system. Beinstingel et al. [14] conducted experimental and numerical studies on the vibration behavior of high-speed planetary gearboxes. Using a rotating lumped parameter model with time-varying gear meshing stiffness, they theoretically investigated instability phenomena and experimentally confirmed the occurrence of parametric instability in planetary gearboxes.

Electromechanical coupling and nonlinear effects in permanent magnet synchronous motors (PMSMs) significantly influence NVH performance and operational safety. Chen et al. [15] established a nonlinear PMSM model that accounts for the unbalanced magnetic pull caused by nonuniform magnetic fields, analyzed and obtained approximate solutions to the vibration equation, and discussed the instability characteristics of the system's vibration response. Shin et al. [16] developed an analytical solution for the magnetic field produced by permanent magnets in PMSMs, analyzed electromagnetic vibration sources such as torque ripple, cogging torque, and radial force density, investigated the motor's vibration characteristics and experimentally validated these findings via vibration tests.

Liu et al. [17] developed a rotor-bearing system model considering unbalanced magnetic pull and rotor eccentricity, using multi-scale perturbation methods to study solution instability. Yang et al. [18] used both finite element and analytical methods to investigate the relationship between electromagnetic forces and vibration modes. Wu et al. [19] proposed a multi-physics model to study motor vibration mechanisms and the influence of current harmonics. Sheng et al. [20, 21] established an electromechanically coupled torsional dynamic model for PMSM rotor systems, studied the system using multi-scale and numerical methods.

While significant research efforts have been devoted to individual motor or gear systems, the coupled vibration phenomena in integrated electric drive systems have received comparatively less attention. Hu et al. [22] developed a transient dynamic model of an integrated system comprising a helical gear transmission and a PMSM, and proposed an active vibration reduction strategy to minimize gear mesh force and dynamic load. Yi et al. [23] established a dynamic model of a motor-driven multistage gear system and analyzed the influence of electromagnetic effects on natural characteristics of the gearbox. Liu et al. [24] investigated the effect of load conditions on natural frequency, vibration modes, and motor current in electric vehicle drive systems under electromagnetic excitations.

This paper focuses on the dynamic behavior of integrated system that consists of a permanent magnet synchronous motor (PMSM) and a two-stage gear train. Considering the influence of the torque angle on the motor's back electromotive force, an analytical expression for the electromagnetic torque is derived using energy principles. A nonlinear torsional dynamic model is established that incorporates both the motor and the gear transmission.

The stability of parametric vibrations induced by time-varying meshing stiffness is analyzed using the multi-scale method. The differential equation of the system is solved numerically via the Runge-Kutta method, and the dynamic characteristics of the elastic meshing force are discussed in both the time domain and the frequency domain. The variations of the dynamic load coefficients for each gear pair with respect to excitation frequency are examined, and the relationship between peak positions and the system's natural frequencies is discussed.

2. Dynamic model of integrated electric drive system

The dynamic model of the integrated electric drive system is composed of a motor module and a gear transmission system module, as illustrated in Fig. 1. Here, the components labeled r , p and g represent the rotor of the permanent magnet synchronous motor, the driving gear, and driven gear, respectively. The synchronous motor r operates at high speed, and after passing through the two-stage meshing gear pairs m_1 and m_2 , the driven gear g_2 delivers high torque and outputs at low speed.

Assuming that the stiffness of the bearing support is significantly greater than that of the gear pair, only torsional vibrations are considered. The torsional displacement of each component is defined as a generalized coordinate of the system:

$$X = [u_r, u_{p1}, u_{g1}, u_{p2}, u_{g2}]^T. \quad (1)$$

In Fig. 1, k_r and k_g represent the torsional stiffness of the motor output shaft and the double gear shaft, respectively, while k_{m1} and k_{m2} represent the mesh stiffness of the two gear pairs. A corresponding convention applies to the damping coefficients, denoted as c_r , c_g , c_{m1} , and c_{m2} .

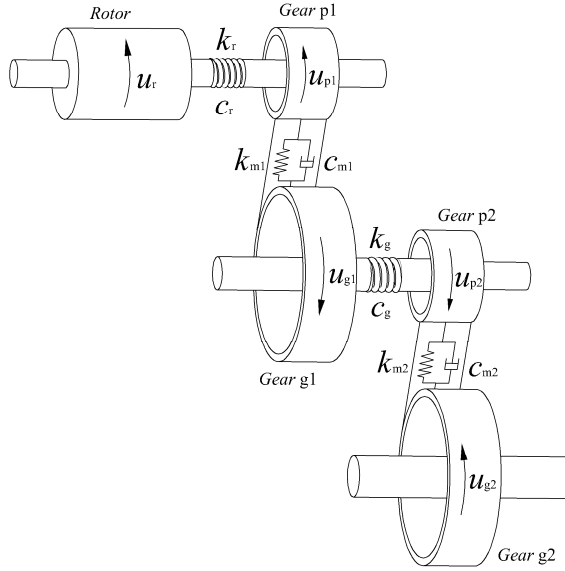


Fig. 1. Torsional dynamic model of the integrated electric drive system

2.1. Electromagnetic excitation of the permanent magnet synchronous motors

2.1.1. Magnetomotive force of the stator

According to the principles of electrical engineering, when a three-phase symmetrical current is supplied, the symmetrical three-phase stator windings produce a resultant magnetomotive force (MMF) with a fundamental component as follows:

$$F_s(\alpha, t) = F_{sm} \cos(\omega_e t - p\alpha) = 1.35 \frac{N_w k_w I_\phi}{p} \cos(\omega_e t - p\alpha), \quad (2)$$

where, F_{sm} represents the fundamental amplitude of the magnetomotive force, ω_e is the current frequency, p denotes the number of pole pairs of the motor, α indicates the relative angle between the centerline of the motor stator yoke and the permanent magnet pole, N_w is the number of series turns per phase winding, and I_ϕ is the effective value of the current. $k_w = k_d k_p$, where k_w is the distribution coefficient of the fundamental winding, k_d is the winding distribution coefficient, and k_p is the winding pitch coefficient. The expressions for k_d and k_p are given as follows:

$$k_d = \frac{\sin\left(\frac{\pi}{2m}\right)}{q \cdot \sin\left(\frac{\pi}{2mq}\right)}, \quad k_p = \sin\left(\frac{y_1}{\tau} \cdot \frac{\pi}{2}\right), \quad (3)$$

where, $q = Z/2pm$ represents the number of slots per pole per phase, where Z is the number of stator slots and m is the number of winding phases. Additionally, y_1 denotes the winding pitch, and τ represents the pole pitch.

2.1.2. Magnetomotive force of the rotor

Taking into account the torque angle resulting from load torque at the rotor, the fundamental magnetomotive force of the permanent magnet rotor when the motor operates under load can be expressed as:

$$F_r(\theta, t) = F_{rm} \cos\left(\omega_e t - p\alpha - (\psi - p\theta) + \frac{\pi}{2}\right) \\ = \frac{4 B_r h_m}{\pi \mu} \sin\left(\frac{\alpha_p \pi}{2}\right) \cos\left(\omega_e t - p\alpha - (\psi - p\theta) + \frac{\pi}{2}\right), \quad (4)$$

where, F_{rm} denotes the fundamental amplitude of the permanent magnet magnetomotive force, B_r refers to the remanent magnetic flux density of the permanent magnet material, μ represents the permeability of the permanent magnet, α_p and h_m are the pole arc coefficient and the magnetization direction thickness of the permanent magnet, respectively, θ is the torque angle of the rotor, and ψ denotes the internal power factor angle.

2.1.3. Synthetic magnetomotive force

The expression for the fundamental synthetic magnetomotive force in the stator coordinate system is given as follows:

$$F(\theta, t) = F_{sm} \cos(\omega_e t - p\alpha) + F_{rm} \cos\left(\omega_e t - p\alpha - (\psi - p\theta) + \frac{\pi}{2}\right). \quad (5)$$

The air gap magnetic field energy of a permanent magnet synchronous motor can be expressed as:

$$W = \frac{Rl}{2} \int_0^{2p\pi} \Lambda(\theta, t) F^2(\theta, t) d\theta = \frac{\pi p R l \Lambda_0}{2} [F_{sm}^2 + F_{rm}^2 - 2F_{sm}F_{rm} \sin(\psi - p\theta)], \quad (6)$$

where l is the effective length of the rotor, R is the average radius of the air gap, $\Lambda_0 = \mu_0/k_u\delta$ denotes the air gap permeance, μ_0 is the vacuum permeability, k_u represents the magnetic saturation coefficient, and δ is the length of the air gap.

By taking the derivative of Eq. (6), the electromagnetic torque of the rotor under load is obtained as:

$$T_e = \frac{\partial W}{\partial(p\theta)} = p\pi R l \Lambda_0 F_{sm} F_{rm} \cos(\psi - p\theta) = F_m [\sin \psi \sin(p\theta) + \cos \psi \cos(p\theta)]. \quad (7)$$

Expanding the trigonometric function containing θ approximately, the electromagnetic torque can be expressed as:

$$T_e = F_m \left(\cos \psi + p \sin \psi \cdot \theta - \frac{1}{2} p^2 \cos \psi \cdot \theta^2 - \frac{1}{6} p^3 \sin \psi \cdot \theta^3 \right) \\ = k_0 + k_1 \theta - k_2 \theta^2 - k_3 \theta^3, \quad (8)$$

where $F_m = p\pi R l \Lambda_0 F_s F_r$, $k_0 = F_m \cos \psi$, $k_1 = p F_m \sin \psi$, $k_2 = \frac{1}{2} p^2 F_m \cos \psi$, $k_3 = \frac{1}{6} p^3 F_m \sin \psi$. Here, k_0 , k_1 , k_2 and k_3 are electromagnetic parameters determined by the motor's structural and operational conditions.

When only the first two components of the steady-state electromagnetic torque are considered, the expression simplifies to:

$$T_e = k_0 + k_1\theta, \quad (9)$$

where, the coefficient k_1 has the same dimension as torsional stiffness and is therefore referred to as the electromagnetic torsional stiffness, denoted as k_e .

2.2. Excitation of gear system parameters

During a single meshing period, the mesh stiffness differs significantly between the single-tooth and double-tooth engagement zones of a gear pair. This abrupt change in stiffness can induce the gear pair to generate noticeable vibration acceleration. In contrast, within either the single-tooth or double-tooth meshing zone, the variation in meshing stiffness is minimal, and this gradual change has a relatively minor influence on the vibration response [25].

Therefore, taking into account the meshing phase, the time-varying meshing stiffness of the gear pair can be expressed as a Fourier series in the following form:

$$k_m(t) = k_m^a + 2k_m^v \sum_{l=1}^{\infty} (a_m^{(l)} \cos(l\Omega_m t) + b_m^{(l)} \sin(l\Omega_m t)). \quad (10)$$

The Fourier coefficients corresponding to Eq. (10) are given by:

$$\begin{aligned} a_m^{(l)} &= \frac{2}{\pi l} \cos[\pi l(2\gamma_m + \epsilon_m)] \sin(\pi l \epsilon_m), \\ b_m^{(l)} &= \frac{2}{\pi l} \sin[\pi l(2\gamma_m + \epsilon_m)] \sin(\pi l \epsilon_m), \end{aligned} \quad (11)$$

where $2k_m^v$ and k_m^a are the fluctuation and mean components of the mesh stiffness, respectively, Ω_m is the meshing frequency, γ_m denotes the meshing phase, and ϵ_m is the contact ratio of the gear pair.

The comprehensive error of gear pair m is defined as follows:

$$e_m(t) = e_{m0} + E_m \sin(\omega_m t + \varphi_m), \quad (12)$$

where e_{m0} is the constant component of the gear pair error, E_m represents the amplitude of the error variation, and φ_m denotes the initial phase of the error.

3. Equations of motion for the system

The vibration differential equation for the integrated electric drive system is derived as follows:

$$\begin{aligned} \frac{I_r}{r_r^2} \ddot{u}_r + \frac{k_r}{r_r} \left(\frac{u_r}{r_r} - \frac{u_{p1}}{r_{p1}} \right) - \frac{k_e}{r_r^2} u_r + \frac{c_r}{r_r} \left(\frac{\dot{u}_r}{r_r} - \frac{\dot{u}_{p1}}{r_{p1}} \right) &= \frac{k_0}{r_r}, \\ \frac{I_{p1}}{r_{p1}^2} \ddot{u}_{p1} - \frac{k_r}{r_{p1}} \left(\frac{u_r}{r_r} - \frac{u_{p1}}{r_{p1}} \right) - \frac{c_r}{r_{p1}} \left(\frac{\dot{u}_r}{r_r} - \frac{\dot{u}_{p1}}{r_{p1}} \right) + k_{m1} \delta_{m1} + c_{m1} \dot{\delta}_{m1} &= 0, \\ \frac{I_{g1}}{r_{g1}^2} \ddot{u}_{g1} - k_{m1} \delta_{m1} - c_{m1} \dot{\delta}_{m1} + \frac{k_g}{r_{g1}} \left(\frac{u_{g1}}{r_{g1}} - \frac{u_{p2}}{r_{p2}} \right) + \frac{c_g}{r_{g1}} \left(\frac{\dot{u}_{g1}}{r_{g1}} - \frac{\dot{u}_{p2}}{r_{p2}} \right) &= 0, \\ \frac{I_{p2}}{r_{p2}^2} \ddot{u}_{p2} - \frac{k_g}{r_{p2}} \left(\frac{u_{g1}}{r_{g1}} - \frac{u_{p2}}{r_{p2}} \right) - \frac{c_g}{r_{p2}} \left(\frac{\dot{u}_{g1}}{r_{g1}} - \frac{\dot{u}_{p2}}{r_{p2}} \right) + k_{m2} \delta_{m2} + c_{m2} \dot{\delta}_{m2} &= 0, \\ \frac{I_{g2}}{r_{g2}^2} \ddot{u}_{g2} - k_{m2} \delta_{m2} - c_{m2} \dot{\delta}_{m2} &= -\frac{T_L}{r_{g2}}, \end{aligned} \quad (13)$$

where, r_r is the radius of the motor rotor shaft; r_p and r_g are the base circle radii of the driving and driven gears, respectively; and I_h (where $h = r, p, g$) represents the rotational inertia of each component. The relative displacements of the gear pair are given by:

$$\delta_{m1} = u_{p1} - u_{g1} - e_{m1}, \quad \delta_{m2} = u_{p2} - u_{g2} - e_{m2}. \quad (14)$$

Substituting Eq. (14) into Eqs. (13) yields the matrix form of the system's differential equation:

$$M\ddot{X} + C\dot{X} + KX = Q, \quad (15)$$

where M , C , K , and Q represent the generalized mass matrix, damping matrix, stiffness matrix, and generalized force vector, respectively. For further details, refer to the Appendix.

4. Decoupling of dynamic equations and stability analysis

Neglecting external excitations and damping, the equation for the system's free vibration is:

$$M\ddot{X} + (K_v(t) + K_a)X = 0, \quad (16)$$

where $K_v(t)$ is the variable stiffness matrix, and K_a is the average stiffness matrix. By setting $K_v(t) = 0$ in Eq. (16), the system equation simplifies to:

$$M\ddot{X} + K_aX = 0. \quad (17)$$

Solving Eq. (17) leads to the eigenvalue problem:

$$K_a\varphi^{(i)} = \omega_i^2 M\varphi^{(i)}, \quad (18)$$

where ω_i and $\varphi^{(i)}$ are the i -th natural frequency and the corresponding mode vector, respectively. Let:

$$X = \Phi q, \quad (19)$$

where $\Phi = [\varphi^{(1)}, \varphi^{(2)}, \dots, \varphi^{(n)}]$ is the main modal matrix, and $q = [x_{q1}, x_{q1}, \dots, x_{qn}]^T$ is the generalized coordinate vector. Substituting Eq. (19) into Eq. (16) and left-multiplying by Φ^T , the regular modal equation of the system is obtained:

$$\Phi^T M \Phi \ddot{q} + \Phi^T K_m^a \Phi q + \Phi^T K_m^v \Phi q = 0. \quad (20)$$

Expanding Eq. (20) gives:

$$\begin{aligned} \ddot{q}_n + \omega_n^2 q_n &+ 2 \sum_{r=1}^L \sum_{l=1}^{\infty} [\varepsilon_{m1} (A_{nr}^{(l)} \cos l \Omega_{m1} t + B_{nr}^{(l)} \sin l \Omega_{m1} t) \\ &+ \varepsilon_{m2} (C_{nr}^{(l)} \cos l \Omega_{m2} t + D_{nr}^{(l)} \sin l \Omega_{m2} t)] q_r = 0, \quad n = 1, 2, \dots, L, \end{aligned} \quad (21)$$

where $\varepsilon_m = \frac{k_m^v}{k_m^a}$, and the coefficient terms are expressed as:

$$\begin{aligned} A_{nr}^{(l)} &= k_{m1}^a a_{m1}^{(l)} \delta_{m1}^{(n)} \delta_{m1}^{(r)}, & B_{nr}^{(l)} &= k_{m1}^a b_{m1}^{(l)} \delta_{m1}^{(n)} \delta_{m1}^{(r)}, \\ C_{nr}^{(l)} &= k_{m2}^a a_{m2}^{(l)} \delta_{m2}^{(n)} \delta_{m2}^{(r)}, & D_{nr}^{(l)} &= k_{m2}^a b_{m2}^{(l)} \delta_{m2}^{(n)} \delta_{m2}^{(r)}. \end{aligned}$$

Using the multi-scale method, time variables representing different scales are introduced:

$$T_0 = t, \quad T_1 = \varepsilon t, \quad (22)$$

where $\varepsilon = \max\{\varepsilon_{m1}, \varepsilon_{m2}\}$. The first-order approximation solution of Eq. (21) is assumed as:

$$q_n(t, \varepsilon) = q_{n0}(T_0, T_1) + \varepsilon q_{n1}(T_0, T_1), \quad n = 1, 2, \dots, L. \quad (23)$$

Substituting Eq. (23) into Eq. (21), and equating terms of the same power of ε yields:

$$q_{n0} = A_n(T_1)e^{i\omega_n T_0} + cc, \quad (24)$$

$$\begin{aligned} D_0^2 q_{n1} + \omega_n^2 q_{n1} &= -2i\omega_n e^{i\omega_n t} D_1 A_n - 2 \frac{\varepsilon_{m1}}{\varepsilon} \sum_{r=1}^L \sum_{l=1}^{\infty} (A_{nr}^{(l)} \cos l \Omega_{m1} t + B_{nr}^{(l)} \sin l \Omega_{m1} t) q_{r0} \\ &\quad - 2 \frac{\varepsilon_{m2}}{\varepsilon} \sum_{r=1}^L \sum_{l=1}^{\infty} (C_{nr}^{(l)} \cos l \Omega_{m2} t + D_{nr}^{(l)} \sin l \Omega_{m2} t) q_{r0}, \end{aligned} \quad (25)$$

where $A_n(T_1)$ is the complex amplitude, and cc denotes the complex conjugate of the preceding term.

Substitution Eq. (24) into Eq. (25) leads to:

$$\begin{aligned} D_0^2 q_{n1} + \omega_n^2 q_{n1} &= -2i\omega_n e^{i\omega_n t} D_1 A_n - \frac{\varepsilon_{m1}}{\varepsilon} \sum_{r=1}^L \sum_{l=1}^{\infty} (A_{nr}^{(l)} - iB_{nr}^{(l)}) (A_r e^{i(\omega_r + l\Omega_{m1})t} + \bar{A}_r e^{i(-\omega_r + l\Omega_{m1})t}) \\ &\quad - \frac{\varepsilon_{m2}}{\varepsilon} \sum_{r=1}^L \sum_{l=1}^{\infty} (C_{nr}^{(l)} - iD_{nr}^{(l)}) (A_r e^{i(\omega_r + l\Omega_{m2})t} + \bar{A}_r e^{i(-\omega_r + l\Omega_{m2})t}) + cc. \end{aligned} \quad (26)$$

From the analysis of the above equation, in addition to the resonance that occurs when the meshing frequency approaches the system's natural frequency, secular terms arise when $l\Omega_m$ approaches the combination frequencies $\omega_n \pm \omega_r$. This behavior indicates that the gear system exhibits an instability region due to parametric excitation.

5. Parameter excitation vibration characteristics

The key parameters for the PMSM module and the two-stage gear transmission module, corresponding to the model in Fig. 1, are provided in Table 1 and Table 2, respectively.

The natural frequencies of the integrated electric drive system, calculated from Eq. (17), are given in Table 3.

5.1. Dynamic characteristics of the meshing force

The differential Eq. (13) are solved numerically using the Runge-Kutta method, yielding real-time solutions for each degree of freedom in the system. The meshing force for gear pair m is calculated as follows:

$$F_m(t) = k_m(t)\delta_m(t) + c_m(t)\dot{\delta}_m(t), \quad (27)$$

where $k_m(t)$ and $c_m(t)$ denote the time-varying meshing stiffness and damping coefficients, respectively.

Table 1. Parameters of the motor module

Parameters	Values	Parameters	Values
Number of phases	$m = 3$	Number of series conductors per phase	$N_w = 80$
Pole pair number	$p = 4$	Number of conductors per slot	10
Number of slots	$Z = 48$	Axial length of stator core (mm)	$l = 100$
Winding pitch	$y_1 = 5$	Axial length of rotor core (mm)	$l = 100$
Polar distance	$\tau = 6$	Remanent magnetic flux density (T)	$B_r = 1.097$
Rotor inner diameter (mm)	$r = 70$	Thickness of permanent magnet (mm)	$h_m = 5$
Rotor outer diameter (mm)	$r = 123.8$	Torsional stiffness (N·m/rad)	$k_r = 2.1 \times 10^5$
Stator inner diameter (mm)	$R = 125$	Width of permanent magnet (mm)	$b = 16$

Table 2. Parameters of the gear transmission

Parameters	Values
Number of teeth	$z_{p1} = 23, z_{g1} = 59, z_{p2} = 25, z_{g2} = 89$
Modulus (mm)	$m_{p1} = m_{g1} = 2, m_{p2} = m_{g2} = 3$
Tooth width (mm)	$b_{p1} = 30, b_{g1} = 30, b_{p2} = 30, b_{g2} = 30$
Pressure angle (°)	$\alpha_{p1} = \alpha_{g1} = 20, \alpha_{p2} = \alpha_{g2} = 20$
Moment of inertia (kg·m ²)	$I_{p1} = 1.03 \times 10^{-4}, I_{g1} = 2.418 \times 10^{-3}$ $I_{p2} = 7.3 \times 10^{-4}, I_{g2} = 7.95 \times 10^{-2}$
Mesh stiffness (N/m)	$k_{m1}^{max} = 614.68 \times 10^6, k_{m1}^{min} = 347.83 \times 10^6$ $k_{m2}^{max} = 640.77 \times 10^6, k_{m2}^{min} = 362.96 \times 10^6$
Contact ratio	$\epsilon_{m1} = 1.68, \epsilon_{m1} = 1.72$
Torsional stiffness (N·m/rad)	$k_g = 9.0 \times 10^5$

Table 3. Natural frequencies of the integrated electric drive system

Order	f_1	f_2	f_3	f_4
Frequency (Hz)	1001.15	3293.81	7868.40	11122.03

Under constant torque conditions and with the motor speed maintained at $n_r = 5000$ r/min, the variation of meshing force with time is illustrated in Fig. 2. The dynamic meshing force oscillates around the static meshing force value, represented by the dashed line. Furthermore, high-frequency fluctuations with small amplitudes are observed within each meshing cycle, which are caused by the time-varying stiffness parameters such as the contact ratio.

With the torque held constant and the motor speed maintained at $n_r = 5000$ r/min, the frequency spectrum of the meshing force is shown in Fig. 3. The results indicate that, in addition to the meshing frequency of the current gear pair, the meshing frequencies of the other gear stage, as well as the system's natural frequencies, are also present in the spectrum of each meshing force. This suggests the occurrence of a coupled multi-frequency vibration phenomenon within the system.

In the frequency spectrum of the meshing force for the high-speed gear pair m_1 , not only does the low-speed meshing frequency f_{m2} (with relatively higher amplitude) appear, but the system's natural frequency and the combined frequency $f_{m1} + f_{m2}$ are also present. Similarly, the high-speed stage meshing frequency f_{m1} also appears in the spectrum of the meshing force F_{m2} of the low-speed stage, though with smaller amplitudes. This frequency domain behavior reveals that the coupling effect between the meshing vibrations of different gear pairs is asymmetric.

This phenomenon occurs because the torsional internal force of the connecting shaft couples the vibration displacements of different frequencies together, which then act on the two connected components separately as force and reaction. The coupled components, in turn, feed back the vibration displacement containing new frequencies to the meshing force of the gear pair in the form of equivalent meshing line deformation. As a result, mutual coupling arises between the meshing forces of different gear pairs.

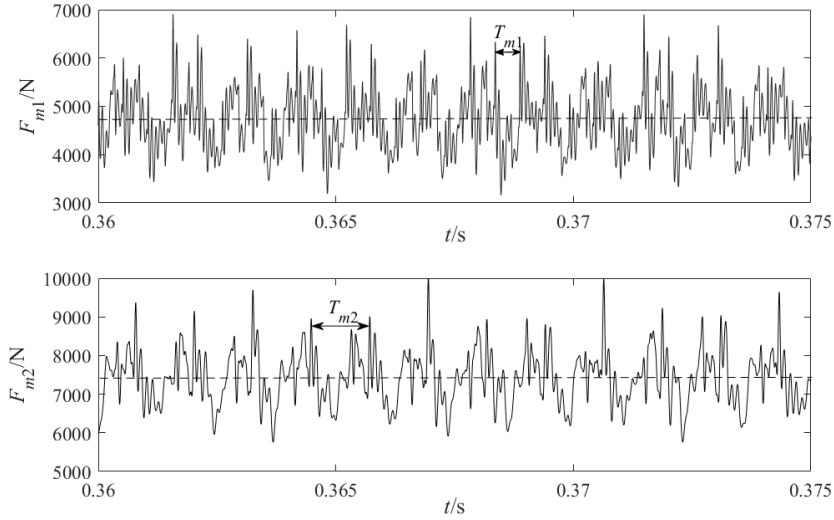


Fig. 2. Dynamic meshing force of gear pair

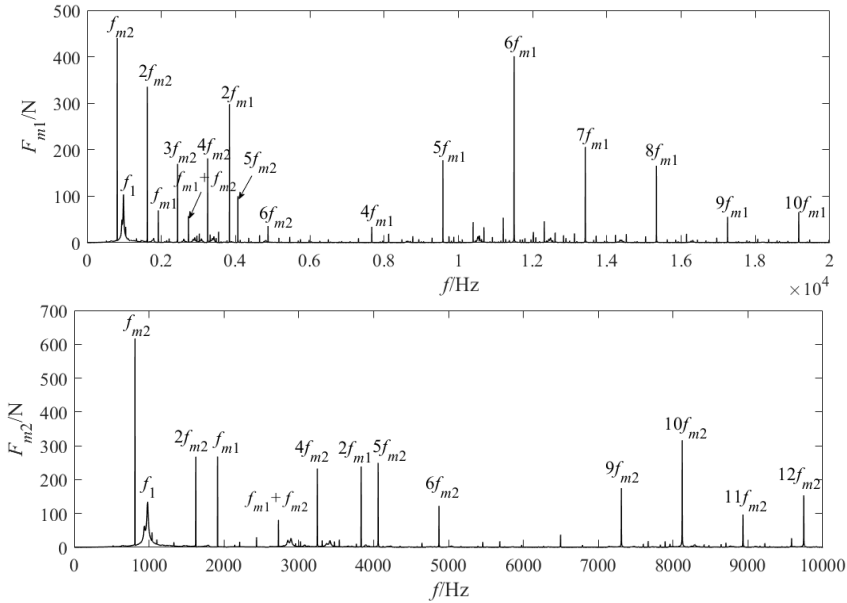


Fig. 3. Spectrum of meshing forces

5.2. Characteristics of dynamic load coefficient

The dynamic characteristics of the gear system, particularly under high-speed operating conditions, have a direct impact on its overall performance. In this study, the dynamic load coefficient is used as an indicator to evaluate the dynamic behavior of the gear transmission system. The dynamic load coefficient $G_m(t)$ is defined as:

$$G_m(t) = \max\left(\frac{F_m(t)}{F'_m}\right), \quad (28)$$

where, $F_m(t)$ denotes the dynamic meshing force, and F'_m represents the static meshing force.

The relationship between the dynamic load coefficient and the meshing frequency is shown in Fig. 4. It can be observed that, within the investigated frequency range, the dynamic load coefficient of gear pair m_1 is significantly higher than that of gear pair m_2 . This is attributed to the higher rotational speed and more pronounced vibration of gear pair m_1 . Furthermore, when the meshing frequency approaches the natural frequency of the system, both dynamic load coefficients G_{m1} and G_{m2} exhibit a sharp increase, which is caused by the strong primary resonance response of the system.

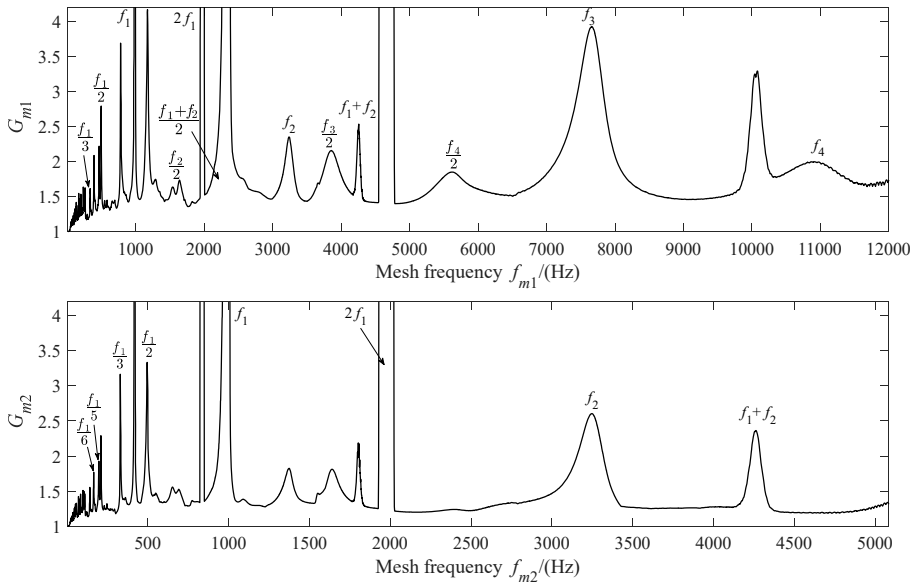


Fig. 4. Dynamic load coefficients of the system

Owing to the time-varying meshing stiffness of the gears, parametric vibrations are excited. The meshing frequencies f_{m1} and f_{m2} induce subharmonic resonance, superharmonic resonance, and additive combination resonance responses in the system.

Specifically, when integer multiples of the meshing frequency (e.g., $2f_{m1}$ or $3f_{m1}$) approach the natural frequencies f_1 or f_2 , superharmonic resonance is observed, resulting in a distinct resonance peak. Similarly, subharmonic resonance occurs when $f_{m1} = 2f_1$ or $f_{m2} = 2f_1$, which is accompanied by a broader resonance region in the vicinity.

When the meshing frequency or one of its harmonics approaches the sum of two natural frequencies, a pronounced additive combination resonance occurs, accompanied by a distinct peak in the dynamic load coefficient. Specifically, resonances at $f_{m1} = f_1 + f_2$ and $f_{m2} = f_1 + f_2$ are directly excited by the fundamental meshing frequency, whereas resonance at $f_{m1} = \frac{(f_1+f_2)}{2}$ is driven by the second harmonic of the meshing frequency.

The time-varying meshing stiffness in multistage gear transmission systems induces parametric excitation and dynamic coupling between different gear pairs, leading to complex resonance phenomena. Effectively addressing these issues requires a systematic and multi-faceted approach focused on shifting critical resonance frequencies outside the operational range, reducing vibration amplitudes, or mitigating their dynamic impact.

By adjusting the stiffness or rotational inertia of relevant components – for example, by modifying the diameter of the intermediate shaft or optimizing the bearing span – the natural frequencies of the system can be effectively adjusted. In addition, through rational design of gear transmission ratios and operating speeds, it can be ensured that all meshing frequencies, along with their harmonics and subharmonics, avoid coincidence with the system's natural frequencies

or their combination frequencies.

The use of high-contact-ratio (HCR) gears contributes to reducing the fluctuation amplitude of mesh stiffness, thereby mitigating parametric excitation effects. Furthermore, increasing system damping can effectively suppress resonance peak amplitudes. The installation of torsional vibration isolators on intermediate shafts can decouple the transmission of vibrational energy along the drive train.

6. Conclusions

This study established a nonlinear torsional dynamic model for an integrated electric drive system comprising a PMSM and a two-stage gear train. Using the multi-scale method and numerical simulations, the parametric instability and vibration characteristics induced by time-varying mesh stiffness were thoroughly investigated. The principal conclusions are as follows:

- 1) In the time domain, the dynamic meshing force oscillates around the static meshing force value, accompanied by high-frequency, small-amplitude fluctuations.
- 2) The frequency spectrum of the meshing force contains not only the meshing frequency of the current gear pair, but also the natural frequencies of the system and the meshing frequencies of other gear pairs.
- 3) Within the frequency range studied, the dynamic load coefficient of high-speed gear pair m_1 is significantly greater than that of the low-speed gear pair m_2 .
- 4) The dynamic load coefficient of the gear pair peaks not only under the primary resonance conditions, but also during subharmonic, superharmonic, and combination resonance responses. In particular, when the meshing frequency approaches twice the first-order natural frequency, the instability regions induced by subharmonic resonance is significantly larger.

The analytical approach developed in this work can be extended and applied to more complex integrated electric drive systems than those considered here, such as systems incorporating permanent magnet synchronous motors coupled with planetary gear transmission mechanisms.

Acknowledgements

This work was financially supported by the National Key Laboratory of Science and Technology on Helicopter Transmission (Grant No. HTL-O-21G09), Natural Science Research Project of Jiangsu Province Colleges and Universities (Grant No. 22KJA460012), 2023 Jiangsu Outstanding Scientific and Technological Innovation Team in Colleges and Universities (Robotic Micro-Servo Control Technology and Applications).

Data availability

The datasets generated during and/or analyzed during the current study are available from the corresponding author on reasonable request.

Author contributions

Donglin Zhang: conceptualization, methodology, software, writing-original draft, project administration, funding acquisition. Rupeng Zhu: visualization, supervision. Luqiang Ma: software, writing-original draft.

Conflict of interest

The authors declare that they have no conflict of interest.

References

- [1] Y. Shen, S. Yang, and X. Liu, "Nonlinear dynamics of a spur gear pair with time-varying stiffness and backlash based on incremental harmonic balance method," *International Journal of Mechanical Sciences*, Vol. 48, No. 11, pp. 1256–1263, Nov. 2006, <https://doi.org/10.1016/j.ijmecsci.2006.06.003>
- [2] M. T. Khabou, N. Bouchaala, F. Chaari, T. Fakhfakh, and M. Haddar, "Study of a spur gear dynamic behavior in transient regime," *Mechanical Systems and Signal Processing*, Vol. 25, No. 8, pp. 3089–3101, Nov. 2011, <https://doi.org/10.1016/j.ymssp.2011.04.018>
- [3] S. Wei, Q. K. Han, X. J. Dong, Z. K. Peng, and F. L. Chu, "Dynamic response of a single-mesh gear system with periodic mesh stiffness and backlash nonlinearity under uncertainty," *Nonlinear Dynamics*, Vol. 89, No. 1, pp. 49–60, Mar. 2017, <https://doi.org/10.1007/s11071-017-3435-z>
- [4] Q. Chen, Y. Wang, W. Tian, Y. Wu, and Y. Chen, "An improved nonlinear dynamic model of gear pair with tooth surface microscopic features," *Nonlinear Dynamics*, Vol. 96, No. 2, pp. 1615–1634, Mar. 2019, <https://doi.org/10.1007/s11071-019-04874-1>
- [5] Z. Cao, Z. Chen, and H. Jiang, "Nonlinear dynamics of a spur gear pair with force-dependent mesh stiffness," *Nonlinear Dynamics*, Vol. 99, No. 2, pp. 1227–1241, Nov. 2019, <https://doi.org/10.1007/s11071-019-05348-0>
- [6] Y.-H. Hu, Q.-G. Du, and S.-H. Xie, "Nonlinear dynamic modeling and analysis of spur gears considering uncertain interval shaft misalignment with multiple degrees of freedom," *Mechanical Systems and Signal Processing*, Vol. 193, p. 110261, Jun. 2023, <https://doi.org/10.1016/j.ymssp.2023.110261>
- [7] J. Lin and R. G. Parker, "Mesh stiffness variation instabilities in two-stage gear systems," *Journal of Vibration and Acoustics*, Vol. 124, No. 1, pp. 68–76, Jan. 2002, <https://doi.org/10.1115/1.1424889>
- [8] J. Lin and R. G. Parker, "Planetary gear parametric instability caused by mesh stiffness variation," *Journal of Sound and Vibration*, Vol. 249, No. 1, pp. 129–145, Jan. 2002, <https://doi.org/10.1006/jsvi.2001.3848>
- [9] G. Liu and R. G. Parker, "Nonlinear dynamics of idler gear systems," *Nonlinear Dynamics*, Vol. 53, No. 4, pp. 345–367, Dec. 2007, <https://doi.org/10.1007/s11071-007-9317-z>
- [10] Z. Rao, C. Y. Zhou, Z. H. Deng, and M. Y. Fu, "Nonlinear torsional instabilities in two-stage gear systems with flexible shafts," *International Journal of Mechanical Sciences*, Vol. 82, pp. 60–66, May 2014, <https://doi.org/10.1016/j.ijmecsci.2014.02.021>
- [11] G. Liu, J. Hong, and R. G. Parker, "Influence of simultaneous time-varying bearing and tooth mesh stiffness fluctuations on spur gear pair vibration," *Nonlinear Dynamics*, Vol. 97, No. 2, pp. 1403–1424, Jun. 2019, <https://doi.org/10.1007/s11071-019-05056-9>
- [12] S. H. Gawande and V. V. Palande, "Half width and phasing method for reduction of instabilities of mesh stiffness variation in two-stage gear," *Australian Journal of Mechanical Engineering*, Vol. 21, No. 3, pp. 815–829, May 2023, <https://doi.org/10.1080/14484846.2021.1914889>
- [13] S. H. Gawande and V. V. Palande, "Reducing instabilities of mesh stiffness variation in two-stage gear using phasing method," *JMST Advances*, Vol. 2, No. 4, pp. 89–101, Sep. 2020, <https://doi.org/10.1007/s42791-020-00035-3>
- [14] A. Beinstingel, R. G. Parker, and S. Marburg, "Experimental measurement and numerical computation of parametric instabilities in a planetary gearbox," *Journal of Sound and Vibration*, Vol. 536, p. 117160, Oct. 2022, <https://doi.org/10.1016/j.jsv.2022.117160>
- [15] X. Chen, S. Yuan, and Z. Peng, "Nonlinear vibration for PMSM used in HEV considering mechanical and magnetic coupling effects," *Nonlinear Dynamics*, Vol. 80, No. 1-2, pp. 541–552, Jan. 2015, <https://doi.org/10.1007/s11071-014-1887-y>
- [16] H.-J. Shin, J.-Y. Choi, H.-I. Park, and S.-M. Jang, "Vibration analysis and measurements through prediction of electromagnetic vibration sources of permanent magnet synchronous motor based on analytical magnetic field calculations," *IEEE Transactions on Magnetics*, Vol. 48, No. 11, pp. 4216–4219, Nov. 2012, <https://doi.org/10.1109/tmag.2012.2200658>
- [17] H. Liu, Y. Wu, X. Wang, P. Yan, and X. Zhang, "Nonlinear normal modes and primary resonance for permanent magnet synchronous motors with a nonlinear restoring force and an unbalanced magnetic pull," *Nonlinear Dynamics*, Vol. 97, No. 2, pp. 1197–1213, Jun. 2019, <https://doi.org/10.1007/s11071-019-05040-3>
- [18] Z. Yang, S. Wang, J. Hong, and J. Li, "Analysis of electromagnetic exciting force and vibration of rotating armature permanent magnet synchronous motor," *The Journal of Engineering*, Vol. 2018, No. 17, pp. 1903–1908, Oct. 2018, <https://doi.org/10.1049/joe.2018.8345>

- [19] Z. Wu, S. Zuo, Z. Huang, X. Hu, S. Chen, and C. Liu, "Modelling, calculation and analysis of electromagnetic force and vibroacoustic behavior of integer-slot permanent magnet synchronous motor considering current harmonics," *Journal of Vibration Engineering and Technologies*, Vol. 10, No. 3, pp. 1135–1152, Feb. 2022, <https://doi.org/10.1007/s42417-022-00434-x>
- [20] L. Sheng, W. Li, G. Xin, Y. Wang, M. Fan, and X. Yang, "Nonlinear torsional vibration analysis and nonlinear feedback control of complex permanent magnet semidirect drive cutting system in coal cutters," *Complexity*, Vol. 2019, No. 1, May 2019, <https://doi.org/10.1155/2019/9359218>
- [21] L. Sheng, W. Li, S. Jiang, J. Chen, and A. Liu, "Nonlinear torsional vibration analysis of motor rotor system in shearer semi-direct drive cutting unit under electromagnetic and load excitation," *Nonlinear Dynamics*, Vol. 96, No. 2, pp. 1677–1691, Mar. 2019, <https://doi.org/10.1007/s11071-019-04878-x>
- [22] J. Hu, T. Peng, M. Jia, Y. Yang, and Y. Guan, "Study on electromechanical coupling characteristics of an integrated electric drive system for electric vehicle," *IEEE Access*, Vol. 7, pp. 166493–166508, Jan. 2019, <https://doi.org/10.1109/access.2019.2953310>
- [23] Y. Yi, D. Qin, and C. Liu, "Investigation of electromechanical coupling vibration characteristics of an electric drive multistage gear system," *Mechanism and Machine Theory*, Vol. 121, pp. 446–459, Mar. 2018, <https://doi.org/10.1016/j.mechmachtheory.2017.11.011>
- [24] K. Liu, W. Wu, S. Yuan, G. Lu, and X. Chen, "Modal characteristics of electric vehicle powertrain considering electromagnetic effect," *Journal of Sound and Vibration*, Vol. 530, p. 116972, Jul. 2022, <https://doi.org/10.1016/j.jsv.2022.116972>
- [25] D. Zhang, R. Zhu, M. Li, W. Tan, and P. Li, "Meshing stiffness parametric vibration of coaxial contrarotating encased differential gear train," *Mathematical Problems in Engineering*, Vol. 2021, pp. 1–13, Feb. 2021, <https://doi.org/10.1155/2021/8950945>

Appendix

$$\begin{aligned}
 M &= \text{diag} \left[\frac{I_r}{r_r^2}, \frac{I_{p1}}{r_{p1}^2}, \frac{I_{g1}}{r_{g1}^2}, \frac{I_{p2}}{r_{p2}^2}, \frac{I_{g2}}{r_{g2}^2} \right], \\
 C &= \begin{bmatrix} \frac{c_r - c_e}{r_2^2} & -\frac{c_r}{r_r r_{p1}} & 0 & 0 & 0 \\ -\frac{c_r}{r_r r_{p1}} & \frac{c_r}{r_{p1}^2} + c_{m1} & -c_{m1} & 0 & 0 \\ 0 & -c_{m1} & c_{m1} + \frac{c_g}{r_{g1}^2} & -\frac{c_g}{r_{g1} r_{p2}} & 0 \\ 0 & 0 & -\frac{c_g}{r_{p2} r_{g1}} & \frac{c_g}{r_{p2}^2} + c_{m2} & -c_{m2} \\ 0 & 0 & 0 & -c_{m2} & c_{m2} \end{bmatrix}, \\
 K &= \begin{bmatrix} \frac{k_r - k_e}{r_2^2} & -\frac{k_r}{r_r r_{p1}} & 0 & 0 & 0 \\ -\frac{k_r}{r_r r_{p1}} & \frac{k_r}{r_{p1}^2} + k_{m1} & -k_{m1} & 0 & 0 \\ 0 & -k_{m1} & k_{m1} + \frac{k_g}{r_{g1}^2} & -\frac{k_g}{r_{g1} r_{p2}} & 0 \\ 0 & 0 & -\frac{k_g}{r_{p2} r_{g1}} & \frac{k_g}{r_{p2}^2} + k_{m2} & -k_{m2} \\ 0 & 0 & 0 & -k_{m2} & k_{m2} \end{bmatrix}, \\
 Q &= \left[\frac{k_0}{r_r} \quad 0 \quad 0 \quad 0 \quad -\frac{T_L}{r_{g2}} \right]^T.
 \end{aligned}$$



Donglin Zhang received Ph.D. degree in College of Mechanical and Electrical Engineering from Nanjing University of Aeronautics and Astronautics, Nanjing, China, in 2021. Now he works at Nanjing Vocational College of Information Technology. His current research interest includes electromechanical transmission system design and dynamics.



Rupeng Zhu received his Ph.D. degree from Nanjing University of Aeronautics and Astronautics, Nanjing, China, in 2000. Now he is professor and doctoral supervisor of College of Mechanical and Electrical Engineering of Nanjing University of Aeronautics and Astronautics and was also the director of the National Key Laboratory of Science and Technology on Helicopter Transmission, engaged in the design of helicopter transmission system.



Luqiang Ma received Ph.D. degree in College of Mechanical and Electronic Engineering from Nanjing Forestry University, Nanjing, China, in 2020. Now he works at Nanjing Vocational College of Information Technology. His current research interest includes mechanical design and advanced manufacturing technology.